

## **Abstract**

This paper outlines the process of building and testing a Mach-Zhender Interferometer optical setup that employs phase modulation for the purpose of testing the Deep Phase Modulation technique for recent improvements in the signal processing of the interferometric signals. The paper will discuss the interferometer assembly and all its components, as well as the signal processing technique of spectrum analysis through Discrete Fourier Transforms.

# Building and Testing a Phase Modulated Homodyne Mach-Zender Interferometer for Testing Improved Interferometer Signal Processing of the Deep Phase Modulation Technique

---

August 7, 2012

John Karlen

## **1 Introduction**

### **1.1 Experiment Overview**

Almost one century ago, Einstein predicted the existence of waves in the space-time medium, which set in motion the beginnings of what was to become a worldwide search for evidence of these oscillations. In addition to reinforcing General Relativity, the discovery of Gravitational Waves (GW) would open a new stream of information from the stars, which could hold insights to any number of mysteries in the world of physics, and could discover many more.

An important development in the search for gravitational waves has been the effort to construct the Laser Interferometer Space Antenna experiment, which, when completed, would allow visibility of potential GWs at lower frequencies. This would be instrumental in GW analysis, as it would allow for the detection of various phenomena, invisible to ground-based detectors, such as the coalescence of massive black holes, which are too susceptible to seismic noise at these frequencies (mHz-Hz).

## 1.2 Deep Phase Modulation

LISA will most likely employ a Homodyne Deep Phase Modulated Interferometer, a new technique for signal processing, which eliminates some of the inherent complexities in Heterodyne Interferometry instrumentation needed to modulate laser frequency, in favor of the more computationally complex phase modulation with greater dynamic range, needed for the large range of separation between the spacecraft. This is critical for LISA, because it allows the spacecraft to measure the phase of a signal over several fringes, while the modulation can adjust for the motion of the spaceships relative to each other. The compact Deep Phase Modulation Interferometry (DPMI) introduces a sinusoidal modulation frequency into the beam, which leads to a time-dependent interferogram, which is illustrated in figure 1. Figure 1 also schematically depicts the Mach-Zhender interferometer

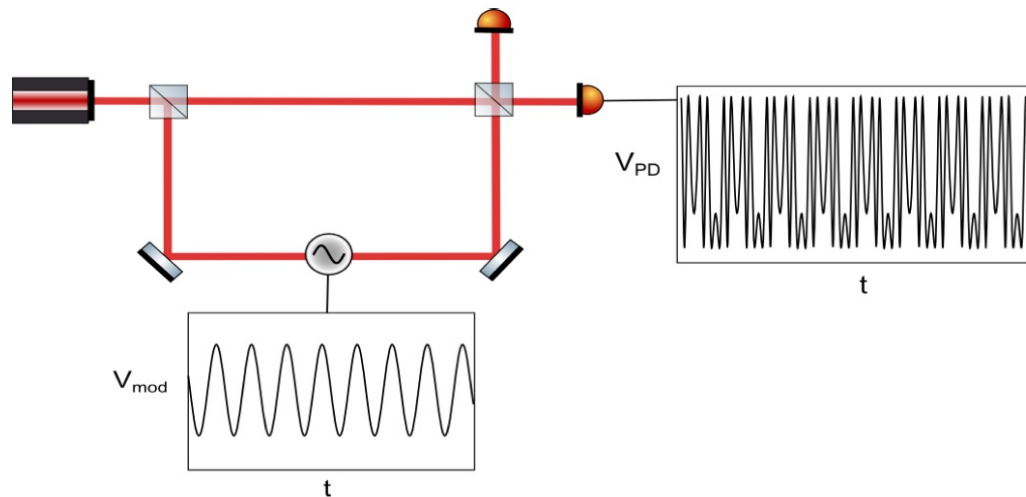


**Figure 1: Modulation Sinusoid and Resulting Interferogram**

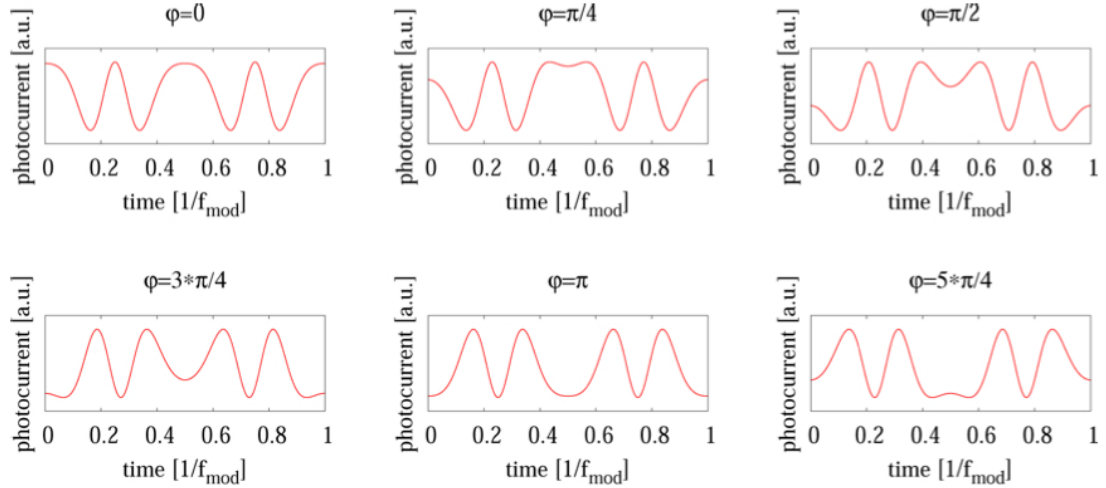


**Figure 2: Waveform of Interferogram showing different values of Phi (interferometer phase)**

When a hypothetical GW causes a change in arm-length, the interferometer phase ( $\phi$ ) will change, because of the optical pathlength difference. The beam that travelled through an altered pathlength will be phase shifted. Our interferometer phase value comes from the difference in phases of the two beams, which gives us our fundamental metric for detection. The various positions of  $\phi$  are illustrated in the modulation patterns of Figure 2.

### 1.3 Implementing DPMI Theory

The output signal is periodic with the modulation frequency and its shape depends on  $\phi$ , as is illustrated. The proposed sensitivity for LISA, using this method, is of the order 20 pm/Hz with an angular resolution of 10rad/ Hz above 3 mHz frequencies [4]. It can be computationally tedious to retrieve arm-length change from the modulate signal, however, with decreasingly expensive computational power this poses less and less of a problem. The new aspect of this approach is its use of larger modulation depths, such as 10 or 20, which allows for greater dynamic range.

We extract the phase from the established “J1 ...J4” method [1-3], which computes the four unknowns of the system, given the height of the harmonics of the modulated signal. The photodiode voltage output

will produce a spectrum with peaks at multiples of the modulation frequency ( $f_{mod}$ ). These peak amplitudes can be expressed in terms of the Bessel functions  $J_n(m)$ , where  $m$  is the modulation depth, or amplitude of  $f_{mod}$ . The output of a phase-modulated homodyne interferometer has the form

$$V_{PD}(t) = A [1 + C \cos(\varphi + m \cos(\omega_m t + \psi))] \quad (1)$$

$V_{PD}$  represents the Photo-Diode Voltage and  $\omega_m = 2\pi f_m$  [4]. We have an arbitrarily large number of these peaks available to us, but we will only require a handful of them to determine the four unknowns, which are  $m$ ,  $\varphi$ , modulation phase ( $\psi$ ) and a common factor ( $k$ ).  $\varphi$  represents the interferometer phase, while modulation phase  $\psi$  represents the phase of the modulation signal, and the  $A$  is determined by nominally constant factors such as light powers and photodiode efficiencies. Contrast depends on factors such as beam alignment; meaning that if two beams don't match up when they reach the diode and their radii are not equal,  $V_{PD}$  will be non-zero at its minimum. The formula for contrast is as follows

$$C = \frac{V_{max} - V_{min}}{V_{max} + V_{min}} \quad (2)$$

Thus, if there is a difference in power between the two beams that arrive at the diode, there will be a contrast  $C \leq 1$  that affects the possible strength of the signal. Equation 1 can be expanded in terms of its harmonic components as

$$V_{PD}(t) = V_{DC}(\varphi) + \sum_{n=1}^{\infty} a_n(m, \varphi) \cos(n(\omega_m t + \psi)) \quad (3)$$

with

$$a_n(m, \varphi) = k J_n(m) \cos\left(\varphi + n \frac{\pi}{2}\right) \quad (4), \text{ and}$$

$$V_{DC}(\varphi) = A(1 + C J_0(m) \cos(\varphi)) \quad (5)$$

Where  $k = 2CA$ , and  $J_n(m)$  are the Bessel functions. In order to produce spectra from the voltage time-series, the series is split into sections of length  $N$ , which are Fourier transformed. Here,  $n = 1 \dots N - 1$ , meaning we produce  $N$  harmonic amplitudes  $a_n$ , where  $a_0$  represents the DC component  $V_{DC}$ , which is not used for the purposes of our experiment. These harmonic amplitudes are complex and their imaginary component is determined by the modulation phase. To compute the real magnitudes, we use the following relation

$$\alpha_n(m, \varphi) = a_n(m, \varphi)e^{in\psi} \quad (6)$$

however, the measured amplitudes  $\tilde{\alpha}(m, \varphi)$  contain an imaginary part because of errors and distortions in the analog electronics which can't perfectly calculate the modulation phase. To determine the four unknowns from our harmonics, we need a least-squared algorithm to efficiently calculate the unknowns, given more measured values than unknowns.

The OROPM program, written by Felipe Guzmán Cervantes, Antonio García Marín, Vinzenz Wand and Gerhard Heinzl, was used to do the analysis on the signal resulting from the interferometer I built, however, it was important to have a thorough understanding of the theory which was being applied to the interferometer output, in order to conceptualize the experiment. I also spent a large amount of my time configuring and compiling software to allow for this data processing; included in this software was a program, NISAM, used to quickly check the raw signal from the interferometer. Familiarity with these software tools was instrumental in building and testing the interferometer.

## 2 Experimental Setup

### 2.1 Optical Bench

I was responsible for assembling the optical Mach-Zhender Interferometer, and the analog processing thereof. We began by splitting

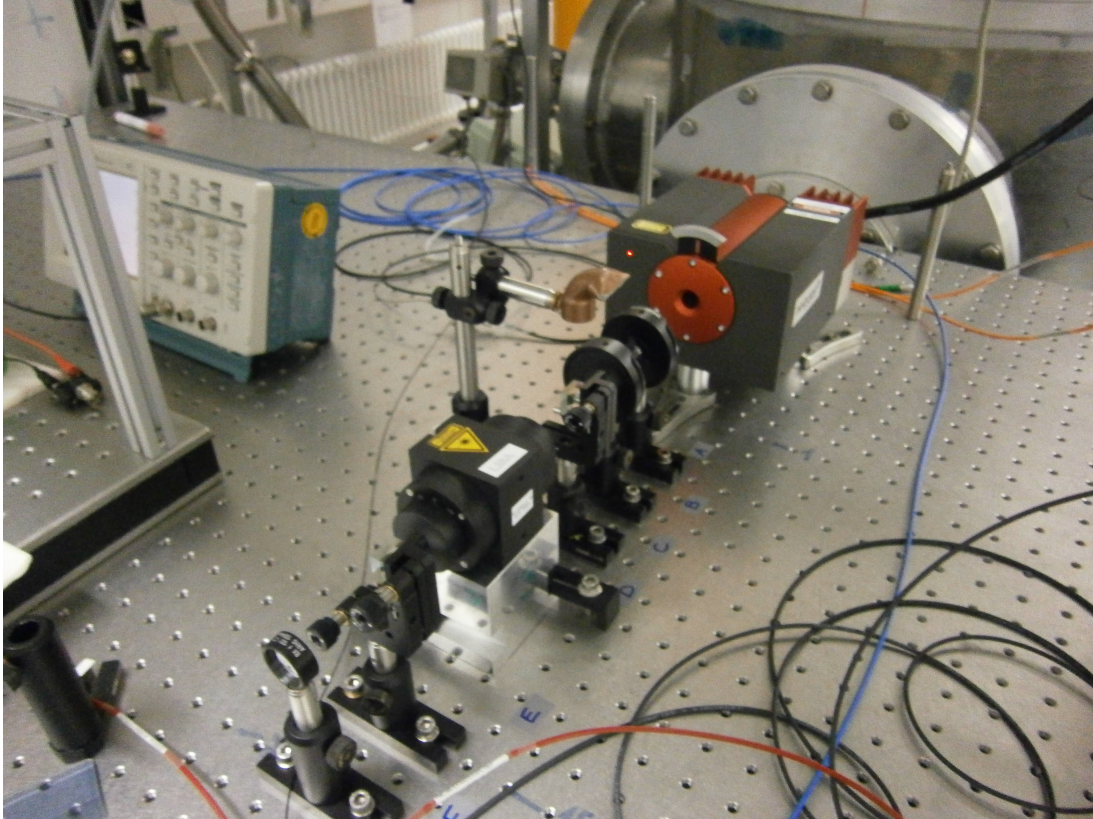


**Figure 3: A non-planar ring oscillator (NPRO) Nd:YAG laser producing 300 mW at 1064 nm was used as light source. The optics in front of the laser clean the beam and prevent reflection back into the laser, which could harm the diode.**

a non-planar ring oscillator (NPRO) Nd:YAG laser, producing 300 mW at 1064 nm (shown in figure 3), and recombining the beam, as shown in figure 6A (A schematic depiction of the Breadboard is shown in figure 6A). The laser beam is first routed through, and split by, optical fibers before it enters the optical bench Breadboard. This allows us to use the interferometer as a modular unit, which can be replaced, after testing, by the optical bench in vacuum, which is the test model optical bench for LISA pathfinder. The two beams are put through Piezoelectric Transducers (PZT), pictured in figure 5, where changing the pathlength modulates the beam phase. When we apply a signal generator to the PZT, we can insert our modulation frequency.

After the PZTs, the beams exit the optical fibers through a fiber collimator and are joined by the beam splitter (BS). The mirror on the bottom right of figure 4 reflects the lower laser into the BS, where the

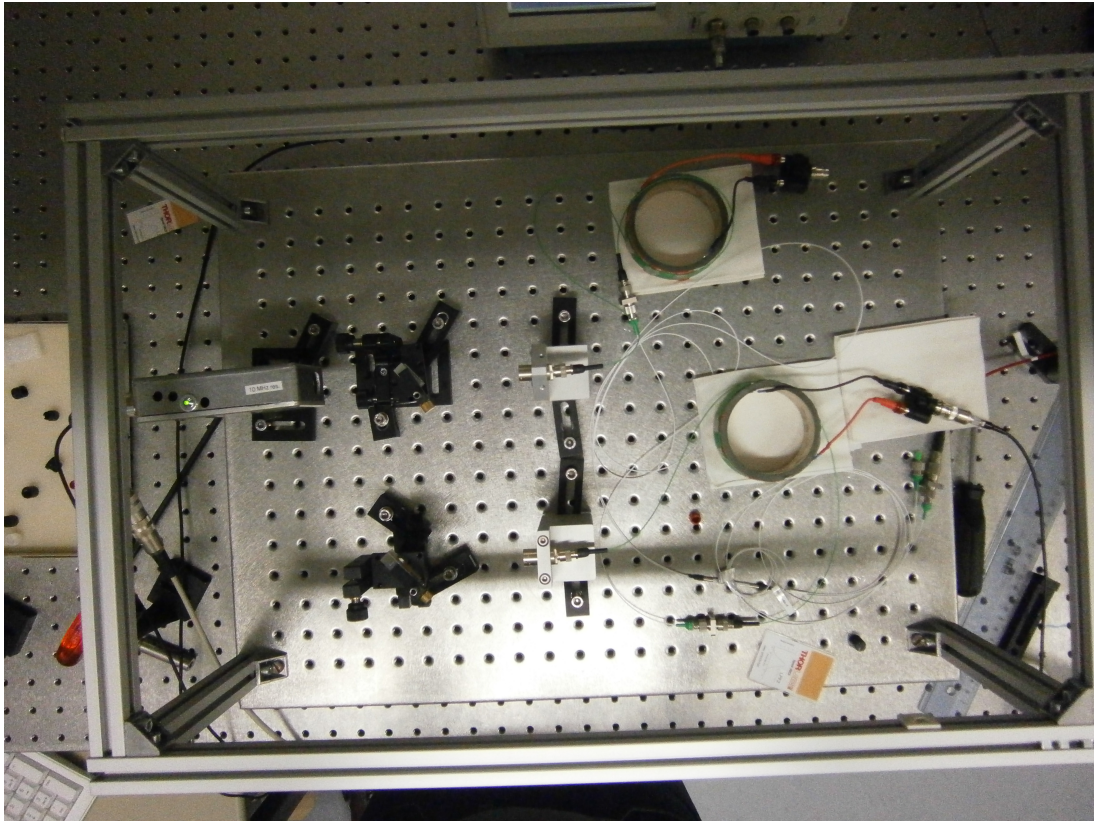


**Figure 4: after an optical fiber beam splitter splits the beam, the two beams enter the PZTs on the right of the board. The free beams are then recombined in the beam splitter, which has two resultant beams with interference, read by the photodiode (grey box on the left).**

BS produces two phase modulated, interfered beams, which have a phase difference of  $\pi$ . Figure 4 shows one photodiode, receiving one of the beams (the grey box at the top left of the Breadboard). The second photodiode for the other resultant beam is not yet installed in figure 4, but would be directly above the beam splitter (at its other output). Figure 5 shows the PZT, a component, which consists of a piezo-electric ceramic ring, a material called HS/HT, wrapped by optical fibers. A voltage is applied to change the ring radius, stretch the fiber loops, and therefore the pathlength of the beam, thereby allowing us to modulate the phase with the voltage from the Numerically Controlled Oscillator (NCO), or signal generator.

Although two PZTs are present on the Breadboard in figure 4, the NCO only applied voltage to one of them, for the duration of my work. The reason for a PZT on each beam is to make optical pathlength

comparable and to anticipate the possibility of injecting test signals or implementing optical pathlength stabilization with the second PZT. The tissues under the PZTs and the BNC voltage input serve to insulate the components from the breadboard, in particular the BNC adaptor, because it is not grounded. During beam alignment, we had to adjust the pitch and yaw of the mirrors to align the beam, while paying attention to

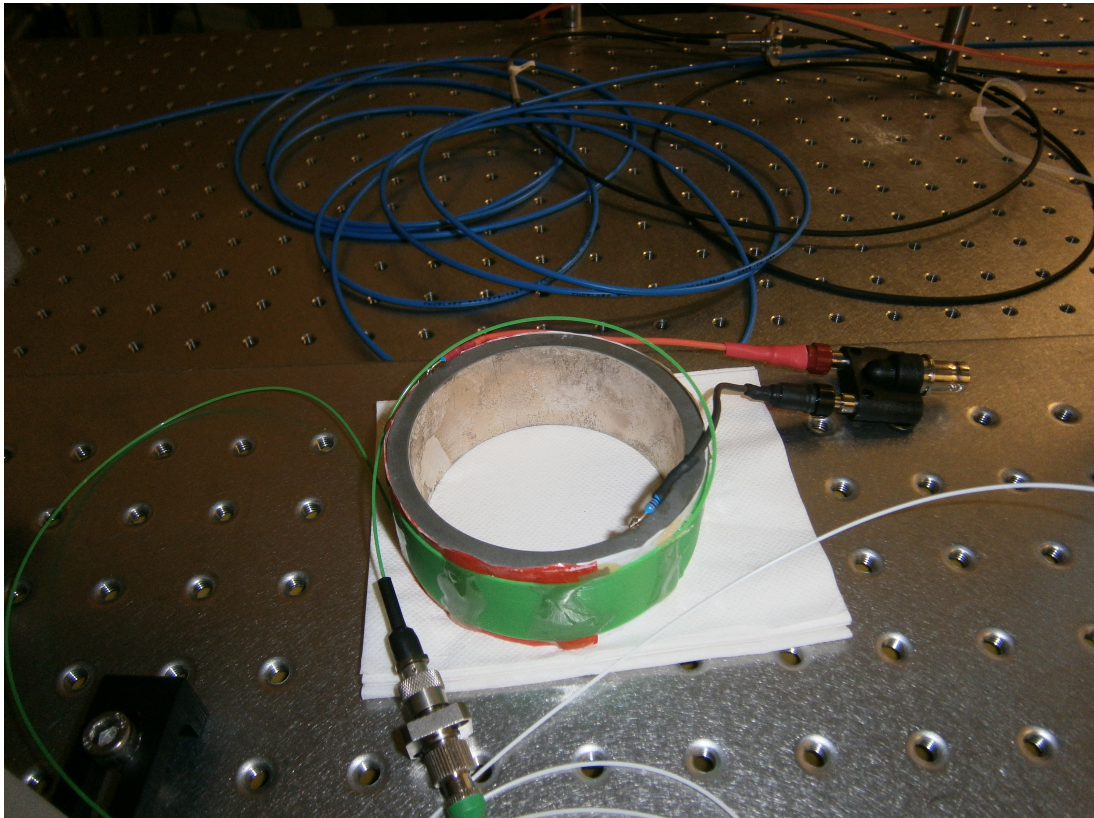


**Figure 5: PZT fiber optic cables wrapped around a metal ring. The positive and negative wires apply the voltage from the NCO across the ring. The negative black wire on the inside, and the positive red wire on the outside apply the voltage across the ring. The white cable is one output of the fiber beam splitter and it is connected to the green PZT optical fiber by the beam joiner at the bottom of the image.**

scattered light. Imperfections in the mirrors and BS, as well as the fiber optic beam splitter, may have caused some of the scattered light, which we were not able to put into the diodes. With the indicator cards, some scattered light could be found, but not eliminated. The main concern about scattered light and beam alignment was the power lost by either beam, before the diode received it, which would contribute to the contrast.

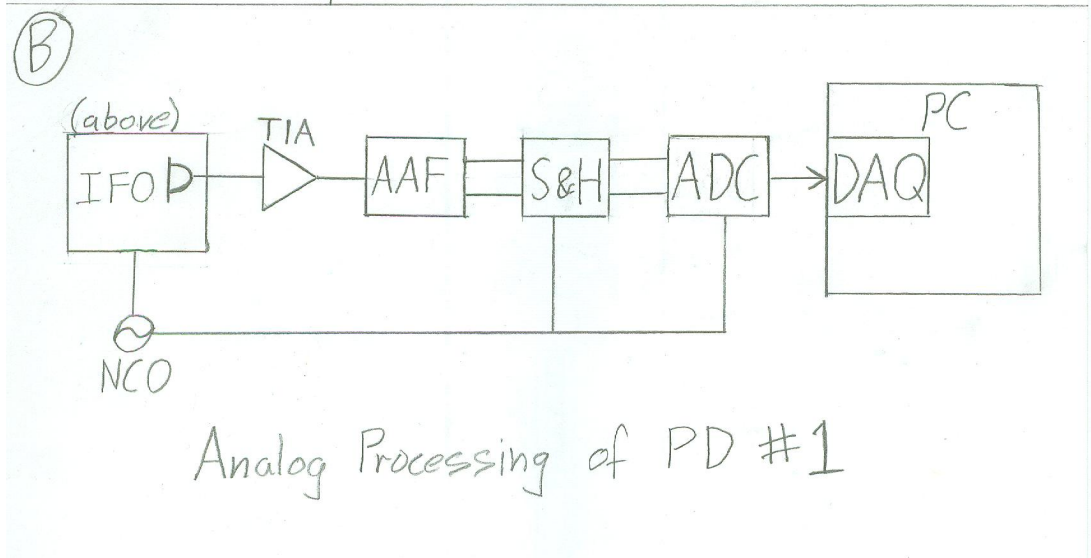
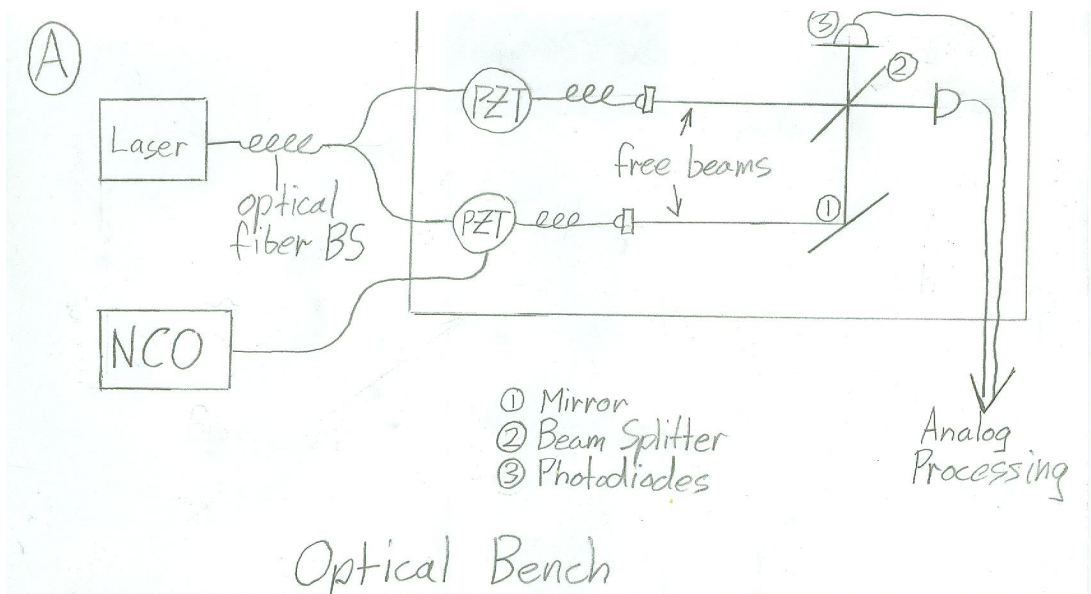


**Figure 6A: Optical Bench with Input and Output.**

**Figure 6B Analog Processing Schematic of one photodiode output**

## 2.2 Analog Processing Setup

Figure 6A shows a schematic depiction of the Breadboard and figure 6B shows the analog processing thereof. The signal to be processed from the

photodiode in the interferometer (IFO) enters a Transimpedance Amplifier (TIA), which will allow us to measure the Transfer Function later. The TIA leads to an Anti Alias Filter to eliminate the aliases above the Nyquist Frequency. This is essentially a low-pass filter. The signal is then split into two streams for noise analysis. The difference between these two streams will produce a null measurement to illustrate the noise resultant from one Photodiode. These two streams are then passed to the sample and hold (S&H), which will take the eventual 4 outputs (one from each photodiode) and hold the signal in each channel according to an external trigger, and then pass them to the Analog-to-Digital Converter (ADC). This ensures that, although the ADC samples its channels serially, it will acquire simultaneous measurements of the signal. The ADC passes the signal to the Data Acquisition Card (DAQ), in the PC, which will deliver the signal to the PC for the DFT and other digital processing. A problem arises, however, if we do not synchronize the ADC to the NCO because the DFT to be applied assumes a continuous periodic signal, and if the ADC is not coherently sampling within the period, the DFT will show noise from the truncated periods. We inject a modulation frequency of 280 Hz at  $4.5 V_{\text{peak-peak}}$  and install another NCO to be externally triggered by the primary one, so that we have another output, this time at 100 kHz, for the S&H and the ADC, which is coherent to the 280 Hz modulation frequency.

### **3 Data Processing and Discrete Fourier Transforms**

#### **3.1 Theory**

In order to observe a coherent signal at some frequency, we need to sample at a frequency of at least twice that frequency. This maximum observable frequency, given a certain sampling frequency  $f_{\text{samp}}$ , is the Nyquist frequency ( $f_{\text{Ny}}$ ), and the relation goes like

$$f_{\text{Ny}} = \frac{f_{\text{samp}}}{2} \quad (7)$$

Assuming that there aren't any frequencies equal to or higher than the Nyquist frequency in our signal, all aliases caused by sampling will occur above the Nyquist frequency. This is the reason we apply an appropriate Anti Aliasing Filter to the signal. Given our constant  $f_{\text{samp}}$  at 100 kHz we have a time-series of equidistant samples from the ADC to process. The goal of the Discrete Fourier Transform (DFT) is two graphs, one of a linear spectrum and the other of a linear spectral density. The Equivalent Noise Bandwidth (ENBW) factor relates them to each other. The power spectrum and spectral density are also noteworthy, and can be found by squaring the linear spectral density or spectrum, but are not as accessible as their linear counterparts, because the linear graphs mirror the amplitude of the injected signal and noise in  $V$  or  $V/\sqrt{Hz}$ . The two spectra can also be expressed in decibels, usually during transfer function investigations. The decibel (dB) is a log ratio of a value to some reference amplitude (1 V in our case). The rms fluctuation of the linear spectrum can be determined from the linear spectral density by integrating over the frequency range. The general method of DFT transforms a vector of  $N$  complex numbers  $x_k$ ,  $k = 0 \dots N-1$ , into another vector of  $y_m$ ,  $m = 0 \dots N-1$ , though in our case, we will take a vector of real numbers and produce a vector of complex numbers [4]. We will be employing the DFT to achieve an amplitude vs. frequency graph from a time series of amplitude, or rather, many time series, each of length  $N$ . The basic forward DFT definition is as follows:

$$y_m = \sum_{k=0}^{N-1} x_k \exp\left(-2\pi i \frac{mk}{N}\right), \quad m = 0 \dots N - 1 \quad (8)$$

For the purposes of this work, we needed to employ a Fast Fourier Transform (FFT) package, which computes the transform approximation in a computationally efficient manner. The specific package used to compute  $y$  was from the FFTW library. Because the input time series is always real, the first and second halves of the output will be complex conjugates of each other, meaning we only require half of them. This means we have  $N/2$  complex values for our spectrum and, therefore,  $N/2$  non-negative real amplitudes.

An important concern, when analyzing spectra is our frequency resolution, defined by

$$f_{res} = \frac{f_{samp}}{N}, \quad (9)$$

where  $f_{res}$  represents the width of a frequency bin, so that it's size determines how many distinct peaks we can see. Maximizing sampling frequency is one of the main concerns of this experiment because my task was to replicate the optical setup of previous experiments for tests with higher sampling frequency, and with the eventual goal of replacing the analog processing components with a field programmable gate array.

### 3.2 Window functions

The reason for synchronization of the modulation frequency to the sampling frequency also plays into the post-processing of the signal. The OROPM software applies window functions to the time series to mitigate discontinuities. In order to apply a DFT, we can apply a window function to each section of  $N$  samples of the time series. Since the DFT expects a continuous signal, we taper the ends of each section of  $N$  samples to zero to eliminate any discontinuities in the signal, and overlap these window functions in a manner illustrated in figure 7. After the window function is applied, we normalize the results to account for the loss in amplitude, and average over many overlapped sections. The window function applied is a type of transfer function  $a(f)$ , at a certain frequency offset.

Many different possible window functions can be used, each of which has a compromise between side lobe amplitude and usable bandwidth. Sidelobes are the undesirable peaks in the spectrum, which are next to the peak spectrum. We can show how the window function isolates a peak frequency, and suppresses sidelobe frequencies by looking at figure 8, the Hanning Window Function in the frequency domain. We want to reduce the level of the sidelobes, however, increasing the suppression increases the bandwidth of the window function. A bandwidth, which is too high is undesirable, as it will cause information from the sidelobes to leak into the central peak. Thus, a

compromise must be made between sidelobe suppression and error in the central peak. For this reason, there are a variety of window functions, which can be applied depending on the signal to noise ratio of the signal (its tolerance for noise leakage).

As an example, I'll discuss the Hanning window, shown in figure 9, which has three windows applied to a time series. It is defined as follows:

$$\omega_j = \frac{1}{2} \left[ 1 - \cos \left( \frac{2\pi*j}{N} \right) \right]; j = 0 \dots N - 1, \quad (10)$$

where  $\omega_j$  is the value of the window function to be applied to the correct time series value  $x_j$ . The window function is symmetric, so that

$$\omega_j = \omega_{N-j}$$

in order to normalize, after the window function had been applied, we define the following two sums:

$$S_1 = \sum_{j=0}^{N-1} \omega_j \quad S_2 = \sum_{j=0}^{N-1} \omega_j^2 \quad (11)$$

These values are used to calculate the normalized power spectrum, or the square of the room-mean-square voltage as follows:

$$PS_{rms}(f_m = m * f_{res}) = \frac{2*|y_m|^2}{S_1^2}; m = 0 \dots \frac{N}{2}, \quad (12)$$

where PS is the rms power spectrum, m is the bin number,  $f_m$  is the frequency of the bin, and  $y_m$  is the amplitude of the bin. Next, we can make use of  $S_2$  to calculate the rms power spectral density as follows:

$$PSD_{rms}(f_m = m * f_{res}) = \frac{2*|y_m|^2}{f_{samp}*S_2}; m = 0 \dots \frac{N}{2}, \quad (13)$$

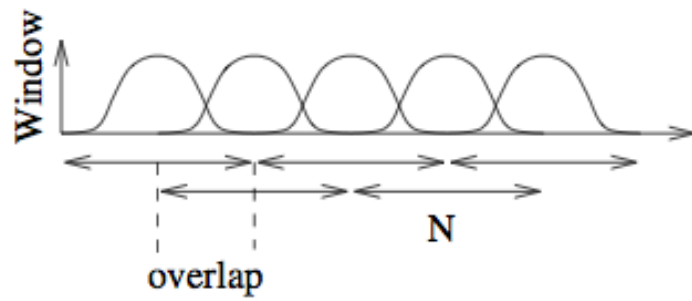


Figure 7: Segmented data stream with window and overlap source: [4]

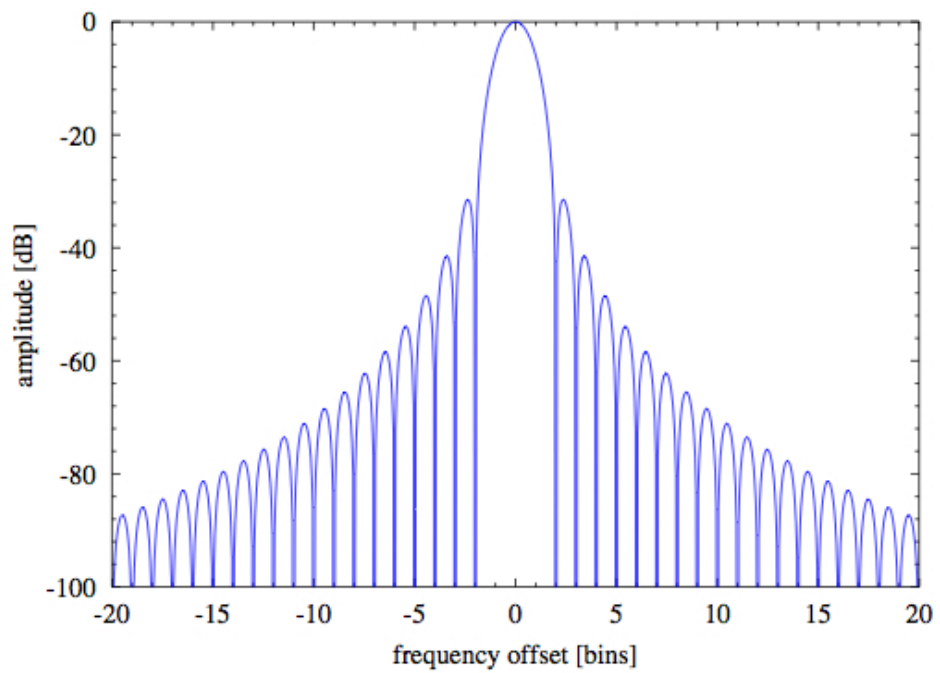


Figure 8: Hanning Window Function source [4]

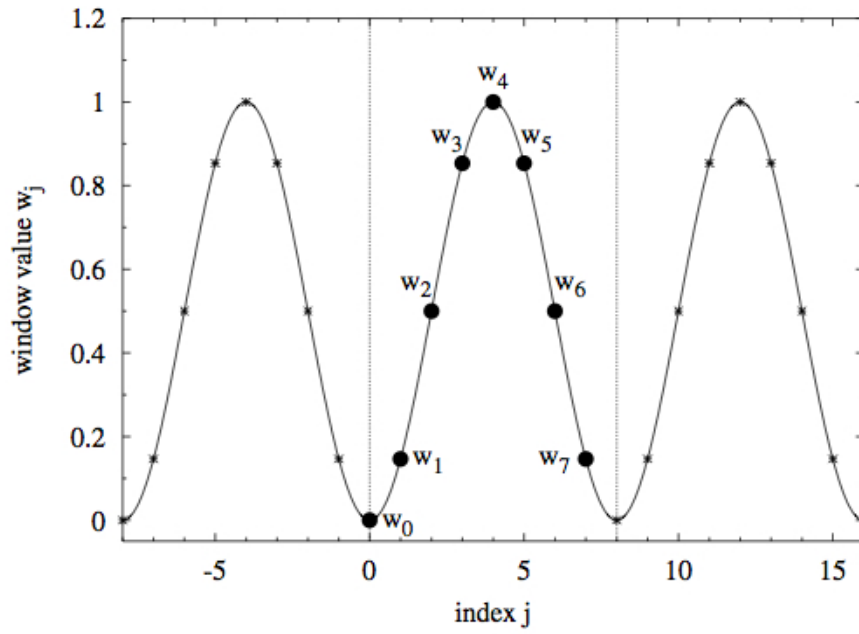


Figure 9: Hanning Window applied to a time series. (no overlap). source: [4]

## **4. Testing and Configuration**

### **4.1 Initial Results**

After assembling the optics and configuring all the programs, we were able to take time-series several hours long. The first data run was taken without analog processing (no AAF or S&H), and with diodes, which had integrated TIAs. After this run, we installed the analog processing and took another data set. The lowering of the noise floor caused by the analog processing and synchronization can be seen in figure 10 (the difference between the red and blue data). These are the results of a null measurement, achieved by subtracting the phase of two outputs, from one photodiode (we produce two outputs by splitting the BNC cable), and taking a spectrum of the results. This gives us the noise in one of the diodes.

After installing the analog processing, we replaced the original photodiodes with quadrant photodiodes and standalone TIAs so that we could measure the transfer function of with the circuit, shown in figure 14. The green data in figure 10 shows the null measurement spectrum after we replaced the diodes with quadrant diodes and a standalone TIAs.

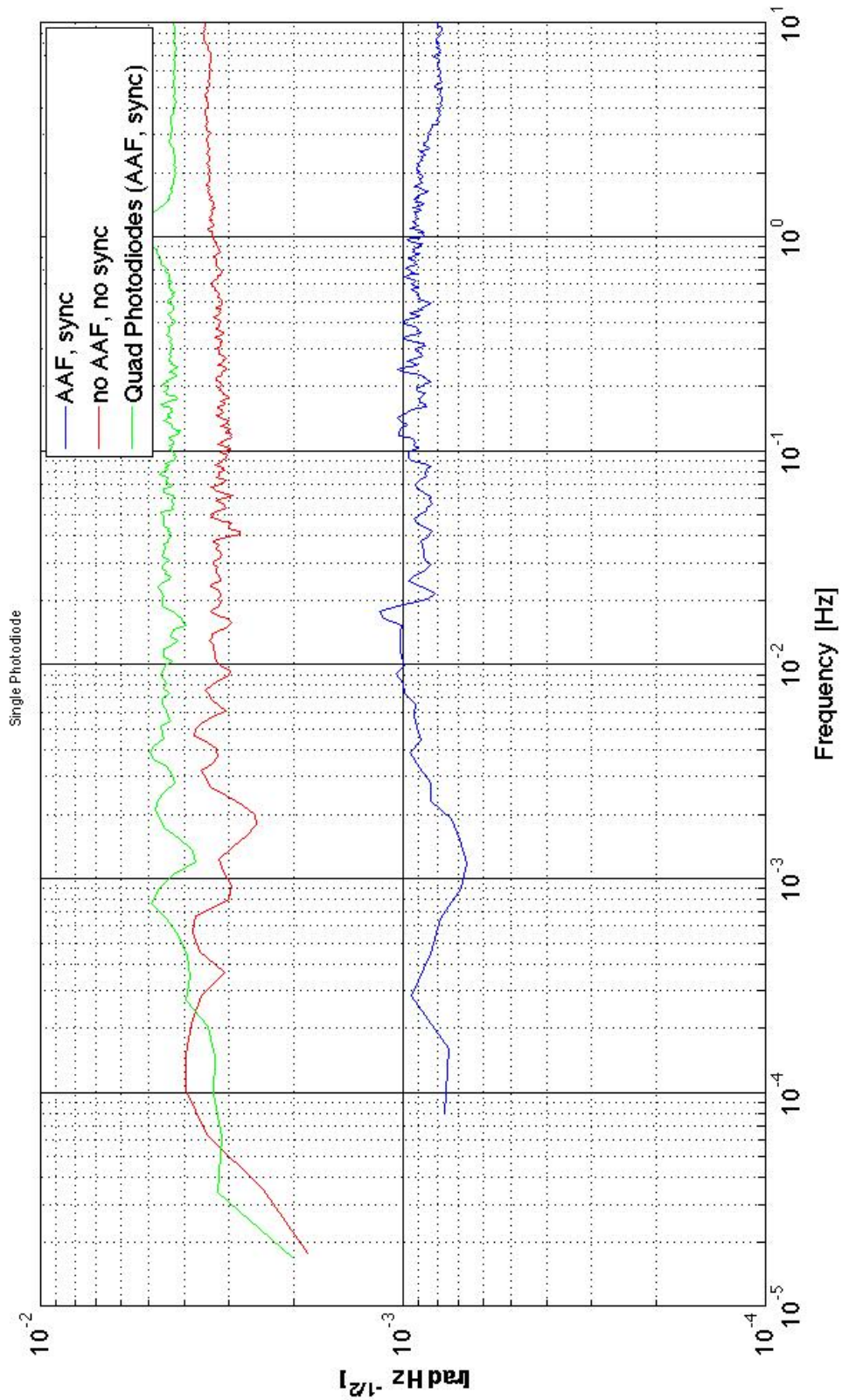
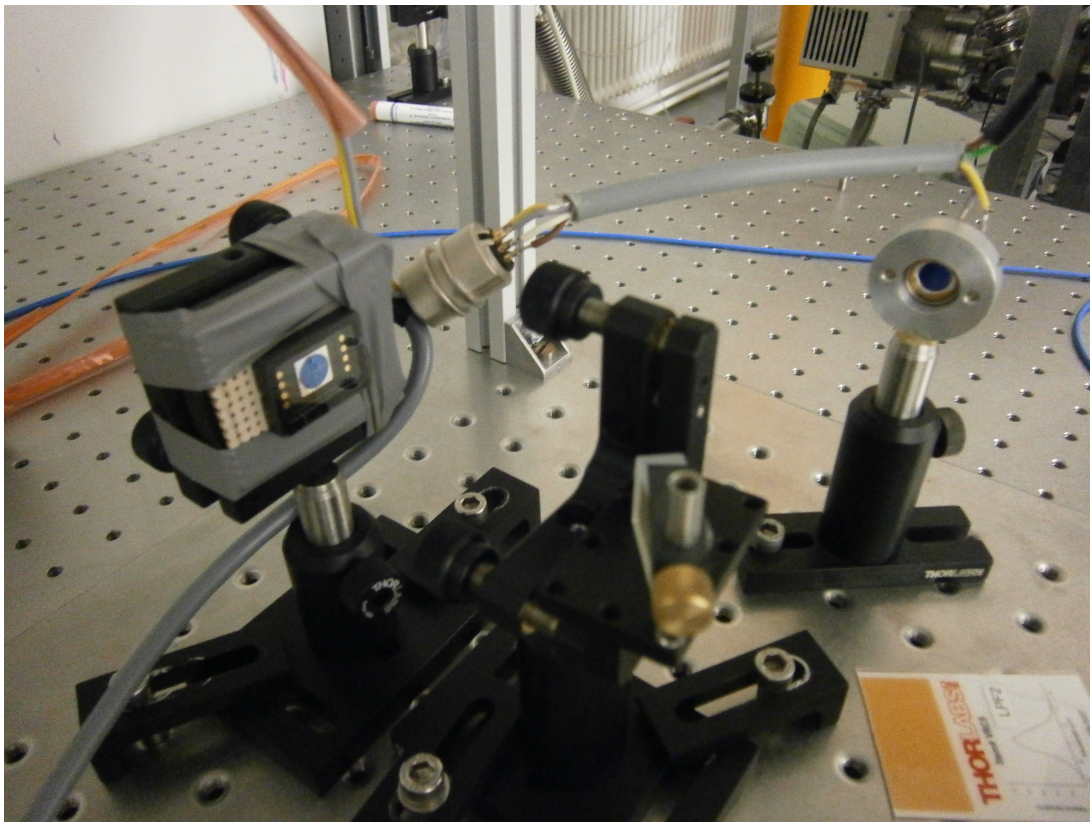


Figure 10: Spectral Density of the null measurement before analog processing (red), after (blue), and with quadrant diodes (green). The AAF and synchronization improved the noise floor significantly, however, the progress was undone by the quadrant photodiodes and standalone TIA being added to the circuit



**Figure 11: Both Quadrant Photodiodes installed, at both BS outputs**

Unfortunately, the noise level increased to above its original value, which could have been caused by the standalone TIA's in the circuit (the analog processing and synchronization were still operational). The quadrant photodiodes can be seen in figure 11; a picture of the BS and its two outputs, received by the diodes.

After examining the noise floor of the null measurement, we can check the quality of our data by comparing the difference of the phase in the two diodes to  $\pi$ , because the signal is reflected by one output of the BS and transmitted by the other, causing one signal to be the mirror image of the other, which, as can be seen in figure 2, means a difference of  $\pi$  in the phase. Therefore, we take the phase of the two outputs and subtract to show the result in figure 12, which, as expected, is in the vicinity of  $\pi$ .

Now that we know that our data is reliable, we can take a look at the spectrums of the interferometer output. Figure 13 shows the data from the

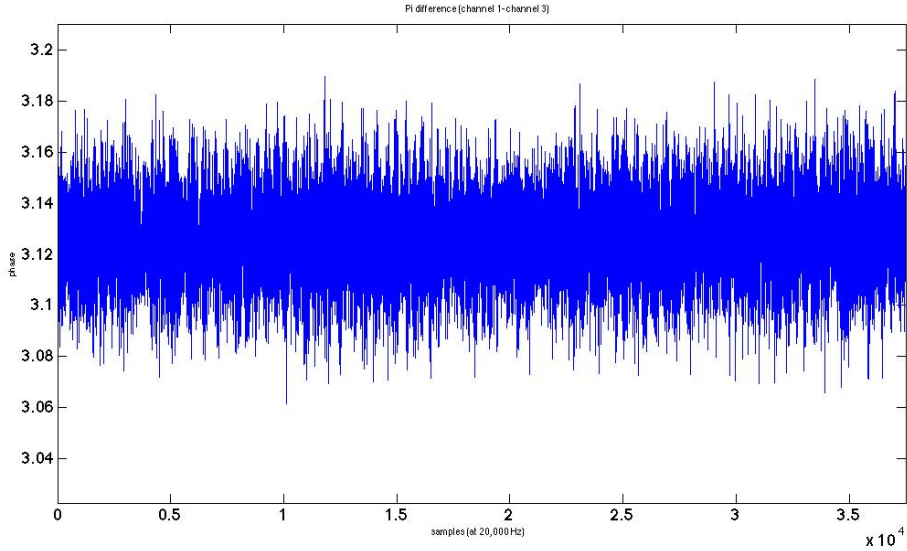


**Figure 12: Pi difference of two photodiodes**

same runs as figure 10, however, the improvement caused by the analog processing and synchronization are not as apparent, and the loss of sensitivity due to the replacement of the diodes is even more apparent. The improvement of the analog processing is most apparent in the range from 1 to 10 Hz.

The large loss in sensitivity due to the new diodes may have been due to beam alignment because one of the quadrant photodiodes only had one operational quadrant, which may not have received the entire power of the beam. This issue was unfortunately, not resolved.

## 4.2 Transfer Functions

The analog processing gives us a much better noise floor, however, it comes at the expense of distortions to the signal due to the increased electronic circuitry, in particular the AAF. This distortion affects each frequency predictably, and each component alters the spectrum of the signal in a predictable way. Fortunately, we can measure this altered spectrum, and account for it in the final analysis. The function, which cancels this effect, is called the Transfer Function (TF), and it has this form:

$$\alpha_n = a_n \gamma_n \quad (14)$$

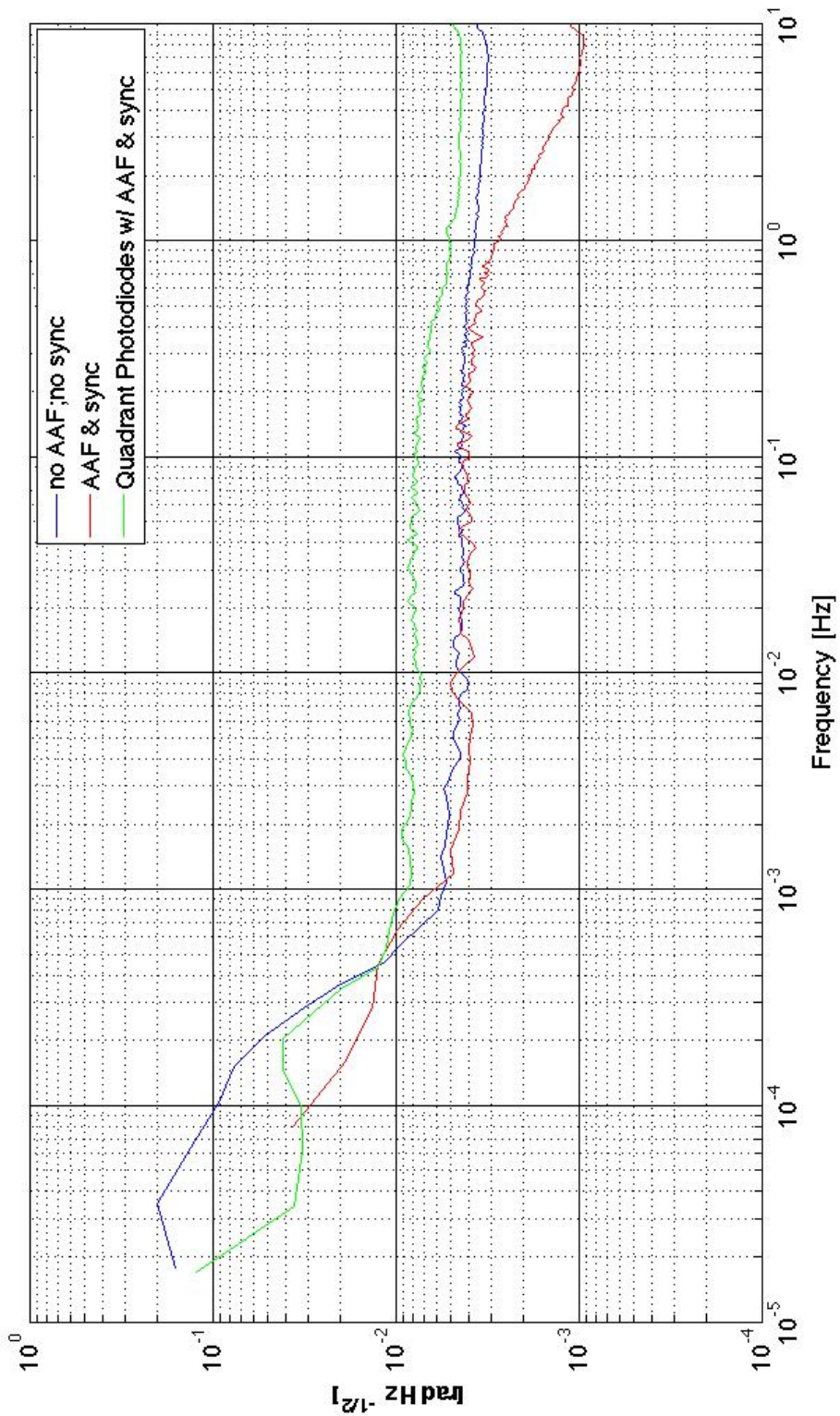
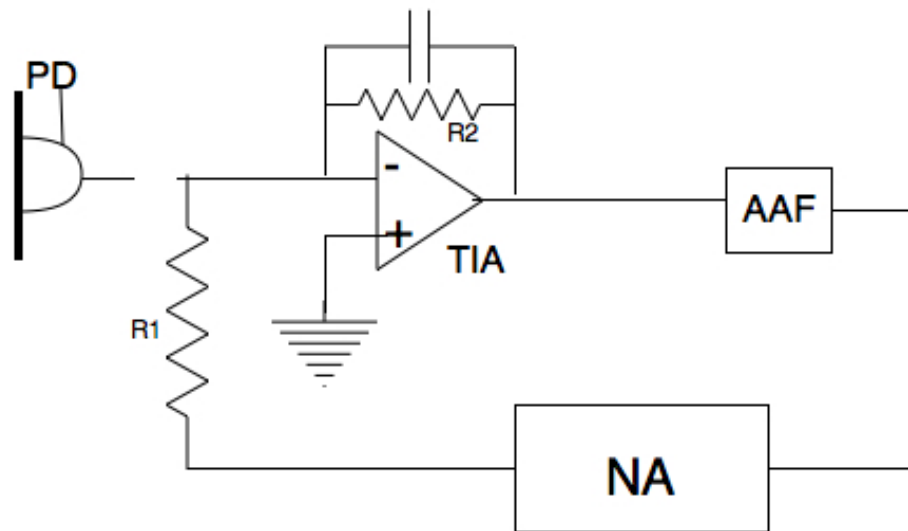


Figure 13: Spectral Density of the interferometer output.

where  $a_n$  is the amplitude of some frequency bin, and  $\gamma_n$  is the TF, at that frequency, which accounts for the distortion. The product,  $\alpha_n$  is the resultant amplitude, after the TF is applied. The large culprits, in terms of TFs, in our setup are the TIA and the AAF. This is the reason for replacing the previous diode boxes, which had built in TIAs, with separate TIAs and diodes. To find the TF of the TIA, without the photodiode, we needed separate electronic components, otherwise, we could not have set up the circuit to measure the TF, as shown in figure 14. The device, which we used to measure the TF is called a Network Analyzer (NA); it produces a sine sweep, which is a sinusoidal voltage that increases its frequency over a specified range. The sweep is applied to a circuit and the NA measures the response as the frequency changes, and produces the spectrum of our transfer function. This process can be applied to individual components, or to a circuit as a whole. The purpose of the TIA is to convert a current, produced by the PD to a voltage. In order to measure the TF of the circuit, we must match the resistance in the TIA with an external resistance. This resistor is needed to inject an electrical signal from the NA, which is always in voltage, but needs to be converted to current. We chose to put the resistor value as the TIA resistor to end up having an amplifier gain of one for the TF measurements (not to alter the TF).

The NA records the TF and it's phase, which improves the estimation of the capability of the modulation phase. As a check of the system, we took TFs of each individual component and multiplied them together to check against the TF of the whole circuit. However, we ran out of time to complete this check, as this was done during the last few days, we had available.



**Figure 14: NA applied to the combined circuit of the AAF and the TIA. The photodiode is shown to illustrate where it would send its signal into the circuit, but is not attached so that the NA can do its job.  $R1 = R2$ .**

The process of estimating transfer functions is detailed in [5].

The transfer function can also be described in the following form:

$$H(s) = \frac{O(s)}{I(s)} \quad (15)$$

where H is the TF, O is the desired output signal, and I is the input unaltered signal.

We had to use two different resistor configurations for R1 in figure 14, because of the fact that one of the quadrant photodiodes only had one operational quadrant. This meant creating 4 resistors in parallel for the diode with all quadrants functioning, and 1 resistor for the photodiode with 1 quadrant. The two resistors I made can be seen in figure 16. Some of the TF's taken from the individual components and their combinations can be seen in figure 15.

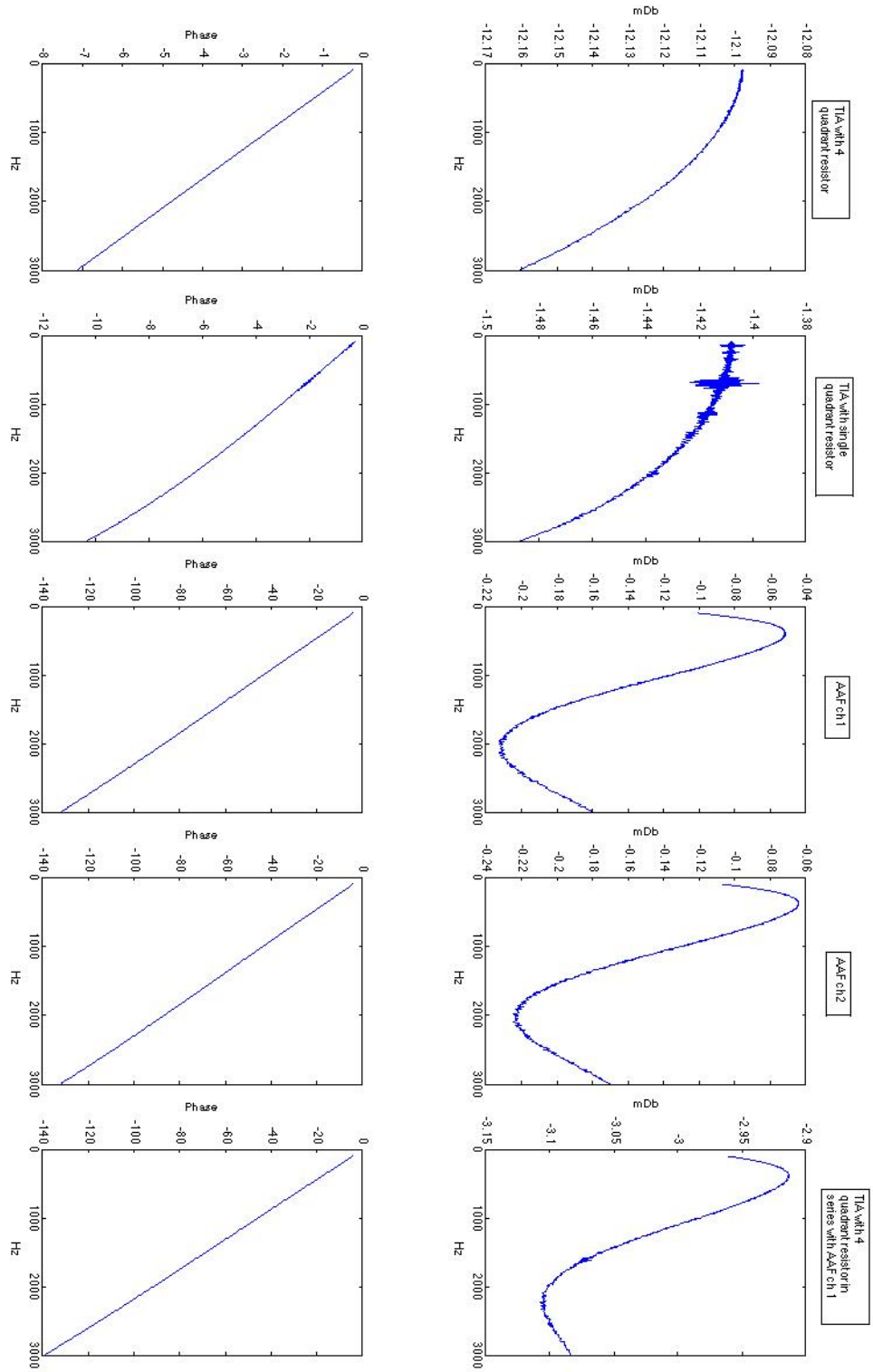


**Figure 15: Various transfer functions taken for individual components (multiple TIAs, one AAF), and their combinations. We also had different resistors for each TIA, due to the different quadrant diodes (one with only one channel of input)**

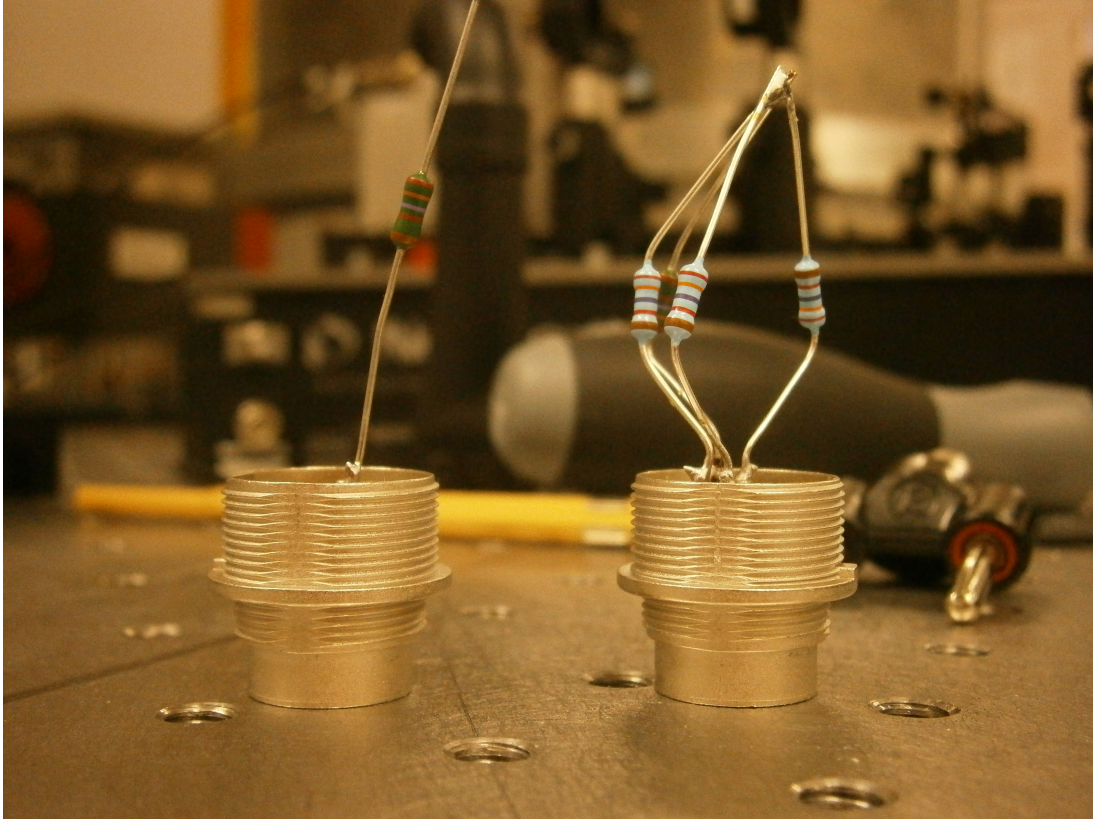


**Figure 16: the left resistor is for the single quadrant photodiode, while the one on the right has four resistors in parallel for the 4 quadrant diode.**

### 4.3 Poles and Zeros

The next step in setting up the interferometer and processing equipment is fitting a model to the aforementioned transfer functions to be applied to any data coming out of the interferometer. We use the poles and zeros model to be able to determine a fit, which characterizes the important points of the transfer functions. The model is as follows:

$$H(f) = A_0 \frac{z_0(f) \dots z_{nz}(f)}{p_0(f) \dots p_{pz}(f)} \exp(-2\pi i f t_{delay}) \quad (16)$$

where  $A_0$  is the overall gain,  $t_{delay}$  is the delay time, whose effect is a phase shift that grows proportional to the frequency. The model characterizes the fit formula with zeros, which initiate a downward turn

in the amplitude as frequency increases, and poles, which do the reverse. A double zero (two zeros at the same location) sharply lowers the function as frequency increases and a double pole sharply raises it. If a pole is given a quality factor, it becomes a peak in the spectrum, where the quality factor determines its width. I used the LISO software package, written by Gerhard Heinzl, to apply a fit to the TF. The literature explaining the use of LISO and the process of determining poles and zeros is the LISO manual [6].

#### References:

1. V. S. Sudarshanam and K. Srinivasan, "Linear readout of dynamic phase-change in a fiber-optic homodyne interferometer," *Opt. Lett.* 14, 140–142 (1989).
2. W. Jin, L. M. Zhang, D. Uttamchandani, and B. Culshaw, "Modified J1 ... J4 method for linear readout of dynamic phase-changes in a fiber-optic homodyne interferometer," *Appl. Opt.* 30, 4496–4499 (1991).
3. V. S. Sudarshanam and R. O. Claus, "Generic J1...J4 method of optical-phase detection: Accuracy and range enhancement," *J. Mod. Opt.* 40, 483–492 (1993).
4. Heinzl G, Guzmán Cervantes F, García Marin AF, Kullmann J, Feng W, Danzmann K. Deep phase modulation interferometry. *Opt. Express.* 18(18):19076-.
5. Heinzl G, Rüdiger A and Schilling R, "Spectrum and spectral density estimation by the Discrete Fourier transform (DFT), including a comprehensive list of window functions and some new flat-top windows" 2002
6. Heinzl G, Garching MPQ, "LISO - Program for Linear Simulation and Optimization of analog electronic circuits – Version 1.61" 1999